RESEARCH PAPER

Semi-analytical solutions for electroosmotic flows with interfacial slip in microchannels of complex cross-sectional shapes

Prakash Goswami · Suman Chakraborty

Abstract In this article, we investigate the implications of electroosmosis with interfacial slip on electrohydrodynamic transport in microchannels having complex (yet symmetric) cross-sectional shapes, by employing a generic semi-analytical approach. We also devise an approximate technique of flow rate prediction under these conditions, using a combined consideration of electroosmotic slip (under thin electrical double layer limits) and Navier slip conditions (originating out of confinement-induced hydrophobic interactions) at the fluid–solid interface. We further assess the effectiveness of the approximate solutions in perspective of the exact solutions, as a parametric function of the relative thickness of the electrical double layer with respect to the channel hydraulic diameter. We illustrate the underlying consequences through examples of elliptic, polygonal, point star-shaped, and annular microchannel cross sections.

List of symbols

A	Area of the channel cross section (m^2)
b	Slip length (m)
D_{h}	Hydraulic diameter of the channel (m)
E	Electric field (V m^{-1})
e	Charge of a proton (C)
e	Eccentricity of ellipse
g	Channel boundary
I_m	Modified 1st kind Bessel functions of order m
K	Non-dimensional EDL thickness
K_m	Modified 2nd kind Bessel functions of order m
k_{B}	Boltzmann constant (J K^{-1})
n	Normal distance from the surface (m)
n_0	Bulk ionic concentration (m^{-3})
n^+	Concentration of cations (m^{-3})
n^-	Concentration of anions (m^{-3})
Q	Volume flow rate in actual situation
Q_{app}	Volume flow rate in approximate situation
T	Absolute temperature (K)
U_{HS}	Helmholtz–Smoluchowski velocity (m s^{-1})
u	Velocity in actual situation (m s^{-1})
u_{app}	Velocity in approximate situation (m s^{-1})
z	Valance

Greek symbols

ρ	Fluid density (kg m^{-3})
μ	Dynamic viscosity (kg m^{-1} s^{-1})
ρ_e	Ionic charge density (C m^{-3})
ε	Permittivity of the medium (C V^{-1} m^{-1})
ψ	EDL potential (V)
ζ	Zeta potential (V)
κ	Reciprocal of EDL thickness (m^{-1})
λ	Eigen value
β	Angle of symmetry (rad.)

P. Goswami
Department of Mathematics, Indian Institute of Technology, Kharagpur, Kharagpur 721302, India

S. Chakraborty (✉)
Department of Mechanical Engineering, Indian Institute of Technology, Kharagpur, Kharagpur 721302, India
e-mail: suman@mech.iitkgp.ernet.in

1 Introduction

Phenomenal advancements in micro-fabrication and the consequent technological promises offered by 'lab on a chip' based microfluidic devices and systems have brought in resurged interests in the investigation of low Reynolds number hydrodynamics over small scales (Stone and Kim 2001; Whitesides and Stroock 2001; Reyes et al. 2002).

Over such length scales, pressure-driven flow actuation may often appear to be rather unattractive, primarily attributable to huge frictional losses and considerable dispersion of the transported samples. Alternative flow actuation mechanisms, therefore, are often considered for flow manipulation and control in devices and systems of these kinds. A handful of such actuation mechanisms exploit interfacial phenomena to a favorable proposition, consistent with the fact that typical microfluidic devices are invariably associated with large area to volume ratios.

Electrokinetic transport happens to provide one of the most popular non-mechanical techniques that utilize favorable interfacial phenomena over small scales for flow actuation and control. Electrokinetic phenomena, in many cases, essentially rely on the formation of a locally non-neutral layer of fluid (also known as the electrical double layer; abbreviated as EDL) adjacent to charged interfaces, in vicinity of which a diffuse cloud of oppositely charged counter-ions effectively screens the surface charge (Hunter 2000). An externally applied electric field may exert a net force on the ionic species located within this charged diffuse layer, which may be transmitted to the incipient fluid by viscous interactions. This, in effect, may lead to a net fluid flow relative to the solid surface. Such flow actuation relative to stationary solid surfaces (also known as electroosmosis), thus, stems from the preferential transport of mobile counterions in the diffuse portion of the EDL in response to an applied electric field. These kinds of flows find wide applications in analytical chemistry (Bruin 2000) and life sciences (Landers 2003; Figeys and Pinto 2001; Dolnik and Hutterer 2001), as evident from a plethora of literature reported on electroosmotic flows over the last couple of decades.

Interestingly, interfacial electrohydrodynamics, responsible for actuating electroosmotic flows, may be intrinsically coupled with 'slipping' hydrodynamics over small scales, marking an apparent deviation from the classical 'no slip boundary condition' based conceptual paradigm. Such interfacial slip may, for example, originate from hydrophobic interactions at the fluid–solid interface. In reality, hydrophobic interactions in narrow confinements may essentially lead to the inception of a less dense phase (often a nanobubble layer of a few nanometers in thickness) in the interfacial region, which shields the outer layer of liquid from being directly exposed to the nearby solid substrate. The intervening depleted phase may essentially act as a low-friction cushion, resulting in an apparent consequence of the slippage of the liquid layer over the confining substrate. It needs to be recognized at this point that such a slip phenomenon is often apparent and not a real one, and is an artifact of an apparent inability in experimentally resolving the flow physics within the nanometer scale less dense fluid layer. In some cases, however, there may occur a real slip at the fluid–solid interface, because of formation of a rarefied layer of gases, or even, a direct slippage of liquid due to characteristically high shear rates prevailing in the interfacial region. Disregarding the underlying physics, such slip phenomena, no matter whether real or apparent, may result in an augmented rate of fluidic transport, as compared to that predicted by the classical no slip-based paradigm. The underlying fluid dynamic consequences may essentially be characterized by a slip length, which is a hypothetical distance up to which the tangent to the velocity profile at the fluid–solid interface may be extrapolated beyond the fluid–solid interface to achieve a condition of zero slip. Researchers conducting independent investigations have reported widely varying slip lengths, starting from tens and hundreds of nanometers to even microns (Zhu and Granick 2002; Bonaccurso et al. 2003; Galea and Attard 2004; Joly et al. 2004). It may further be mentioned in this respect that other factors such as surface roughness and contamination may appear to influence slip-length measurements considerably (Galea and Attard 2004; Joly et al. 2004), from an experimental perspective.

From a conceptual viewpoint, it is important at this stage to recognize that there is a critical demarcation between the standard mathematical treatments of interfacial slip due to hydrophobic interactions (explained as above) and the so-called electroosmotic slip. The later is essentially based on the consideration that typical electroosmotic velocity profiles in microchannels with homogeneous surface conditions are essentially of plug-shape, except for steep velocity gradients within the EDL adjacent to the solid boundary. If the EDL is relatively thin, this gradient is often neglected (i.e., velocity gradients in the EDL are not resolved) for flow computations, and a constant slip velocity instead is postulated at the surface (Dirichlet boundary condition), equating to the velocity in the bulk electroosmotic flow (referred to as 'Helmholtz–Smoluchowski' velocity in the literature) (Li 2004). On the other hand, interfacial slip due to hydrophobic interactions is traditionally represented by a Navier slip condition, in which the slip velocity is expressed as a function of the normal gradient of the tangential velocity component at the interface (essentially a mixed type of boundary condition).

With regard to the possible interactions of electroosmotic slip and Navier slip conditions, it may be noted that the electromechanical phenomena within the EDL and the hydrodynamics of slipping at the interfacial region may be strongly coupled, as attributable to the fact that a net ionic transport may be pumped across the diffuse layer of the EDL in a more prolific manner in the presence of interfacial slip, as manifested through an augmented effective zeta potential. It has been revealed from the previous studies that the interfacial slip, in effect, may lead to an effective zeta potential that is augmented by a factor linearly proportional to the slip length (Joly et al. 2004; Chakraborty 2008). Accordingly, giant amplifications in

the rate of ionic transport within the EDL may be effectively realized with the attainment of a high level of interfacial slippage. Considering such significant scientific and technological implications, Yang and Kwok (2002, 2003, 2004) analyzed the electrokinetic transport through hydrophobic microchannels of simple cross-sectional shapes with Navier slip conditions and obtained the volumetric flow rate analytically using the Debye–Hückel model. In a more recent study, Park and Kim (2009) have introduced a simple method for predicting the altered volumetric transport in electroosmotically driven microchannel flows, using the concept of the Helmholtz–Smoluchowski velocity, by extending the underlying concept to hydrophobic microchannel walls. They have also assessed critically the range of validity of this approach by comparing the results from their formulation with those from the numerical solution of the exact governing partial differential equations.

In the literature, studies on electrokinetic flows with interfacial slip have been traditionally addressed for simple regular geometries. However, in microfluidic devices, one frequently encounters microchannels of more complex cross sections. Such occurrences, in reality, may be natural artifacts of the microfabrication process. For instance, microchannels fabricated by laser ablation on the surface of the polymeric substrate PMMA are likely to exhibit Gaussian-like profiles (Bruus 2008; Park and Lim 2009). The elliptic cross section may also be another channel shape that may be produced by microfabrication (Duan and Muzychka 2007). In many cases, however, cross-sectional irregularities or shape perturbations may be manifested unintentionally during fabrication of other standard-shaped microchannels. In several other cases, the nature of flow passages in arrays of microfluidic pathways gives rise to an effectively more complicated pathway. For example, for a unidirectional flow through a bundle of small parallel packed capillaries of a given radius, the net effect may be a transport through star point family of microchannels (Zhang et al. 2005) in case the fluid flows exterior to the packed capillaries. Considering such geometrical features by going beyond the standard simple geometries commonly addressed in the traditional microfluidics literature, here we outline a general semi-analytical formalism for modeling electroosmotic flows through microchannels having complex (yet symmetric) cross-sectional shapes, subjected to interfacial slip. We also outline a further simplified semi-analytical approach, by considering the combined consequences of the Helmholtz–Smoluchowski velocity and Navier slip velocity in an integrated formalism. We further assess the effectiveness of such simplified considerations for a wide variety of complex cross-sectional geometries (including the ones mentioned as above). Such derivations can serve as a convenient tool for designing electroosmotically driven microfluidics in the presence of hydrophobic interactions in channels with arbitrary yet symmetric cross-sectional geometries, such as those with elliptic, polygonal, point star-shaped, and annular shapes.

2 Mathematical modeling

2.1 Generalized exact solution for microchannels with symmetric cross-sectional shapes

The generalized governing equations of transport for constant density fluids subjected to a combined electroosmotic and pressure-driven flow actuation are given by

$$\nabla \cdot \mathbf{u} = 0 \tag{1}$$

$$\rho \left[\frac{\partial u}{\partial t} + \mathbf{u} \cdot \nabla \mathbf{u} \right] = -\nabla p + \mu \nabla^2 \mathbf{u} + \mathbf{F}_{EK} \tag{2}$$

where $\mathbf{F}_{EK} = \rho_e \mathbf{E}$ is the electrokinetic body force; ρ_e being the ionic charge density and $\mathbf{E}$ being the resultant electric field. In steady state and with low Reynolds number considerations (typical to microscale hydrodynamics), Eq. 2 simplifies to

$$\mathbf{0} = -\nabla p + \mu \nabla^2 \mathbf{u} + \mathbf{F}_{EK}. \tag{2a}$$

Assuming a possible hydrophobic nature of the channel surface, the boundary condition can be given by the Navier slip model

$$\mathbf{u} = b \frac{\partial \mathbf{u}}{\partial n} \bigg|_{boundary} \tag{3}$$

where b denotes the slip length (see Fig. 1).

For a symmetric (z:z) electrolyte, the total ionic charge density, ρ_e, given by

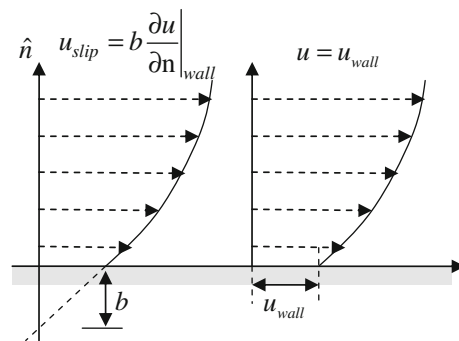$$\rho_e = ez(n^+ - n^-) \tag{4}$$

Fig. 1 Schematic illustration of the paradigm of interfacial slip

where n^+ and n^- are the number densities of cations and anions, respectively, and are given by the Boltzmann distribution (considering no EDL overlap)

$$n^\pm = n_0 \exp\left(\mp \frac{ez\psi}{k_B T}\right) \tag{5}$$

where n_0 is the concentration of ions at the bulk, e is the charge of a proton, z is the valence of ions, k_B is the Boltzmann constant, and T is the absolute temperature. The potential distribution, ψ, inside the EDL, is given by the Poisson equation

$$\nabla^2 \psi = -\frac{\rho_e}{\varepsilon} \tag{6}$$

where ε is the permittivity of the medium. On simplification of (6) with the help of (4) and (5), one may obtain the Poisson–Boltzmann equation in the form

$$\nabla^2 \psi = \frac{2n_0 ez}{\varepsilon} \sinh\left(\frac{ez\psi}{k_B T}\right). \tag{7}$$

Now considering the gradients of EDL potential acting only in the normal direction ($\hat{\mathbf{n}}$) of the boundary, and using the boundary conditions $\psi = \zeta$ at the boundary (assumed to be uniform) and $\psi \to 0$, $\frac{\partial \psi}{\partial n} = 0$, far from the EDL, we have the solution of (7) in the form (Park and Kim 2009), provided that EDLs formed at different surfaces do not interfere:

$$\psi(n) = \frac{4k_B T}{ez} \tanh^{-1}\left[e^{-\kappa n} \tanh\left(\frac{ez\zeta}{4k_B T}\right)\right] \tag{8}$$

where $\kappa = \sqrt{\frac{2n_0 e^2 z^2}{\varepsilon k_B T}}$ is the reciprocal of the EDL thickness, and 'n' is the normal distance of a point inside the EDL from the boundary. For low values of zeta potential, applying the Debye–Hückel linearization the solution (8) takes the form

$$\psi(n) = \zeta e^{-\kappa n}. \tag{8a}$$

For describing the microchannel cross-section contour, we employ a polar coordinate system, as $r = g(\theta)$. The normal distance of a point from the surface of this section is given by: $n = (\mathbf{r} - \mathbf{g}(\theta)) \cdot \frac{-\nabla(r - g(\theta))}{\|\nabla(r - g(\theta))\|}$, where $\mathbf{r}$ is the position vector of a point inside the domain and $\mathbf{g}(\theta)$ is the position vector of a point on the boundary, with respect to the origin (assumed to be located on the channel central axis). Further, we assume fully developed flow along the axial (z) direction, so that $\mathbf{u} = (0, 0, \mathbf{u}(r, \theta))$, $\mathbf{E} = (0, 0, \mathbf{E})$, $\nabla p = \left(0, 0, \frac{dp}{dz}\right)$. In such cases, the momentum Eq. 2a can be written in the form

$$\left[\frac{\partial^2}{\partial r^2} + \frac{1}{r}\frac{\partial}{\partial r} + \frac{1}{r^2}\frac{\partial^2}{\partial \theta^2}\right]\left(u(r, \theta) - \frac{\varepsilon E}{\mu}\psi(r, \theta)\right) = \frac{1}{\mu}\frac{dp}{dz}. \tag{9}$$

The solution of Eq. 9, assuming the finiteness of the solution at the channel central line ($r = 0$), is given by (following Shih 1967; Zhang et al. 2005)

$$u(r, \theta) = \frac{r^2}{4\mu}\frac{dp}{dz} + \frac{\varepsilon E}{\mu}\psi(r, \theta) + r^\lambda(c_1 \cos(\lambda\theta) + c_2 \sin(\lambda\theta)) \tag{10}$$

where λ is an eigen value. For obtaining the complete solution, we consider a p-fold geometry of the microchannel section with fold angle 2β. Symmetricity of the velocity about the line $\theta = 0$(horizontal axis) gives $c_2 = 0$. Further, the condition along $\theta = \beta$, $\frac{\partial u}{\partial \theta} = 0$, gives the eigen values $\lambda = \frac{m\pi}{\beta}$; $m = 0, 1, 2, 3, \ldots$. Then, the solution (10) can be cast in the form

$$u(r, \theta) = \frac{r^2}{4\mu}\frac{dp}{dz} + \frac{\varepsilon E}{\mu}\psi(r, \theta) + \sum_{m=0,1,2,\ldots} c_m r^{\frac{m\pi}{\beta}} \cos\left(\frac{m\pi}{\beta}\theta\right). \tag{10a}$$

The slip boundary condition (3) at the wall reads

$$u(r, \theta)|_{r=g(\theta)} = b(\nabla u \cdot \hat{\mathbf{n}})|_{r=g(\theta)} \tag{10b}$$

where $r = g(\theta)$represents the channel boundary, and $\hat{\mathbf{n}}$ is the unit inward normal to the boundary. This can be simplified as

$$u(g, \theta) = b\left(\sqrt{1 + \frac{g_\theta^2}{g^2}}\right)^{-1}\left(\frac{\partial u}{\partial r} - \frac{g_\theta}{g^2}\frac{\partial u}{\partial \theta}\right)\Bigg|_{r=g} \tag{10c}$$

which gives an equation for the constants c_m as

$$\sum_{m=0,1,2,\ldots} c_m g^{\frac{m\pi}{\beta}-1}\left\{\left[g - b\frac{m\pi}{\beta}\left(\sqrt{1 + \frac{g_\theta^2}{g^2}}\right)^{-1}\right]\right.$$
$$\times \cos\left(\frac{m\pi}{\beta}\theta\right) - b\frac{m\pi}{\beta}\frac{g_\theta}{g}\left(\sqrt{1 + \frac{g_\theta^2}{g^2}}\right)^{-1}\sin\left(\frac{m\pi}{\beta}\theta\right)\right\}$$
$$= -\frac{g^2}{4\mu}\frac{dp}{dz} - \frac{\varepsilon E\zeta}{\mu} + b\left(\sqrt{1 + \frac{g_\theta^2}{g^2}}\right)^{-1}$$
$$\times \left[\frac{g}{2\mu}\frac{dp}{dz} + \frac{\varepsilon E}{\mu}\left(\frac{\partial \psi(g, \theta)}{\partial r} - \frac{g_\theta}{g^2}\frac{\partial \psi(g, \theta)}{\partial \theta}\right)\right]. \tag{11}$$

The boundary condition at $(r_0 = g(0), 0)$ gives

$$c_0 = -\sum_{m=1}^{\infty} c_m r_0^{\frac{m\pi}{\beta}}\left[1 - b\frac{m\pi}{\beta}(r_0^2 + g_\theta^2(0))^{-1/2}\right] - \frac{r_0^2}{4\mu}\frac{dp}{dz} - \frac{\varepsilon E\zeta}{\mu}$$
$$+ br_0(r_0^2 + g_\theta^2(0))^{-1/2}\left[\frac{r_0}{2\mu}\frac{dp}{dz} + \frac{\varepsilon E}{\mu}\frac{\partial \psi(r_0, 0)}{\partial r}\right]$$

substituting Eq. 11 in Eq. 10a, we have

$$u(r,\theta) = \frac{-r_0^2}{4\mu}\frac{dp}{dz}\left(1 - \frac{r^2}{r_0^2} - 2\frac{b}{r_0}\left(1 + \frac{g_\theta^2(0)}{r_0^2}\right)^{-1/2}\right)$$

$$+ \frac{\varepsilon E \zeta}{\mu}\left(\frac{\psi}{\zeta} - 1 + \frac{b}{r_0}\left(1 + \frac{g_\theta^2(0)}{r_0^2}\right)^{-1/2}\frac{r_0}{\zeta}\frac{\partial\psi(r_0,0)}{\partial r}\right)$$

$$+ \sum_{m=1,2,\dots} c_m r_0^{\frac{m\pi}{\beta}}\left\{\left(\frac{r}{r_0}\right)^{\frac{m\pi}{\beta}}\cos\left(\frac{m\pi}{\beta}\theta\right)\right.$$

$$\left. - \left(1 - \frac{b}{r_0}\frac{m\pi}{\beta}\left(1 + \frac{g_\theta^2(0)}{r_0^2}\right)^{-1/2}\right)\right\} \quad (11a)$$

with c_m given by (for $0 < \theta \le \beta$)

$$\sum_{m=1,2,\dots} c_m r_0^{\frac{m\pi}{\beta}}\left[\left(\frac{g}{r_0}\right)^{\frac{m\pi}{\beta}}\left\{\cos\left(\frac{m\pi}{\beta}\theta\right) - \frac{b}{r_0}\frac{r_0 m\pi}{g}\frac{m\pi}{\beta}\left(1 + \frac{g_\theta^2}{g^2}\right)^{-1/2}\right.\right.$$

$$\left.\times\left[\cos\left(\frac{m\pi}{\beta}\theta\right) + \frac{g_\theta}{g}\sin\left(\frac{m\pi}{\beta}\theta\right)\right]\right\}$$

$$\left. - \left(1 - \frac{b}{r_0}\frac{m\pi}{\beta}\left(1 + \frac{g_\theta^2(0)}{r_0^2}\right)^{-1/2}\right)\right]$$

$$= \frac{r_0^2}{4\mu}\frac{dp}{dz}\left[\left(1 - \frac{g^2}{r_0^2}\right) + \frac{2b}{r_0}\frac{g}{r_0}\left(1 + \frac{g_\theta^2}{g^2}\right)^{-1/2}\right.$$

$$\left. - \frac{2b}{r_0}\left(1 + \frac{g_\theta^2(0)}{r_0^2}\right)^{-1/2}\right]$$

$$+ \frac{\varepsilon E \zeta}{\mu}\frac{b}{r_0}\frac{r_0}{\zeta}\left[\left(1 + \frac{g_\theta^2}{g^2}\right)^{-1/2}\left(\frac{\partial\psi(g,\theta)}{\partial r} - \frac{g_\theta}{g^2}\frac{\partial\psi(g,\theta)}{\partial\theta}\right)\right.$$

$$\left. - \left(1 + \frac{g_\theta^2(0)}{r_0^2}\right)^{-1/2}\frac{\partial\psi(r_0,0)}{\partial r}\right]. \quad (11b)$$

In case of low values of zeta potential, applying the Debye–Hückel approximation, we have from Eq. 7, the equation for the potential distribution in cylindrical polar coordinates as

$$\left[\frac{\partial^2}{\partial r^2} + \frac{1}{r}\frac{\partial}{\partial r} + \frac{1}{r^2}\frac{\partial^2}{\partial\theta^2} - \kappa^2\right]\psi = 0. \quad (12)$$

Solving Eq. 12 with the boundary condition $\psi(r,\theta) = \zeta$ and the condition $\frac{\partial\psi}{\partial\theta} = 0$ at $\theta = 0, \beta$, we get

$$\psi(r,\theta) = \sum_{l=0,1,2,\dots} \gamma_l I_{\frac{l\pi}{\beta}}(\kappa r)\cos\left(\frac{l\pi}{\beta}\theta\right) \quad (13)$$

where γ_l are given by

$$\zeta = \sum_{l=0,1,2,\dots} \gamma_l I_{\frac{l\pi}{\beta}}(\kappa r_i)\cos\left(\frac{l\pi}{\beta}\theta_i\right). \quad (13a)$$

After some simplification, Eqs. 13 and 13a can be combined together, to yield

$$\frac{\psi}{\zeta} = \frac{I_0(\kappa r)}{I_0(\kappa r_0)} - \sum_{l=1}^{\infty}\gamma_l'\left\{\frac{I_0(\kappa r)}{I_0(\kappa r_0)} - \frac{I_{l\pi/\beta}(\kappa r)}{I_{l\pi/\beta}(\kappa r_0)}\cos\left(\frac{l\pi}{\beta}\theta\right)\right\} \quad (14)$$

where $\gamma_l' = \gamma_l\frac{I_{l\pi/\beta}(\kappa r_0)}{\zeta}$ and are given by

$$1 = \frac{I_0(\kappa g)}{I_0(\kappa r_0)} - \sum_{l=1}^{\infty}\gamma_l'\left\{\frac{I_0(\kappa g)}{I_0(\kappa r_0)} - \frac{I_{l\pi/\beta}(\kappa g)}{I_{l\pi/\beta}(\kappa r_0)}\cos\left(\frac{l\pi}{\beta}\theta\right)\right\}. \quad (14a)$$

Using the non-dimensional variables $\bar{r} = \frac{r}{D_h}$, $\bar{r}_0 = \frac{r_0}{D_h}$, $\bar{g} = \frac{g}{D_h}$, $\bar{b} = \frac{b}{D_h}$, $\bar{u} = \frac{u}{U_P}$, $\bar{\psi} = \frac{\psi}{\zeta}$, $K = \kappa D_h$, $\bar{U}_E = -\frac{\varepsilon\zeta E}{\mu U_P}$ (where D_h is the hydraulic diameter of the channel, and $U_p = \frac{-D_h^2}{4\mu}\frac{dp}{dz}$) in the above equations, a dimensionless form of the velocity profile is given by

$$\bar{u}(\bar{r},\theta) = \bar{r}_0^2\left(1 - \frac{\bar{r}^2}{\bar{r}_0^2} - 2\frac{\bar{b}}{\bar{r}_0}\left(1 + \frac{\bar{g}_\theta^2(0)}{\bar{r}_0^2}\right)^{-1/2}\right)$$

$$- \bar{U}_E\left(\bar{\psi} - 1 + \bar{b}\left(1 + \frac{\bar{g}_\theta^2(0)}{\bar{r}_0^2}\right)^{-1/2}\frac{\partial\bar{\psi}(\bar{r}_0,0)}{\partial\bar{r}}\right)$$

$$+ \sum_{m=1,2,\dots} c_m'\left\{\left(\frac{\bar{r}}{\bar{r}_0}\right)^{\frac{m\pi}{\beta}}\cos\left(\frac{m\pi}{\beta}\theta\right)\right.$$

$$\left. - \left(1 - \frac{\bar{b}}{\bar{r}_0}\frac{m\pi}{\beta}\left(1 + \frac{\bar{g}_\theta^2(0)}{\bar{r}_0^2}\right)^{-1/2}\right)\right\} \quad (15)$$

where $c_m' = c_m\frac{\bar{r}_0^{\frac{m\pi}{\beta}}}{U_P}$, and are given by the equation

$$\sum_{m=1,2,\dots} c_m'\left[\left(\frac{\bar{g}}{\bar{r}_0}\right)^{\frac{m\pi}{\beta}}\left\{\cos\left(\frac{m\pi}{\beta}\theta\right) - \frac{\bar{b}}{\bar{g}}\frac{m\pi}{\beta}\left(1 + \frac{\bar{g}_\theta^2}{\bar{g}^2}\right)^{-1/2}\right.\right.$$

$$\left.\times\left[\cos\left(\frac{m\pi}{\beta}\theta\right) + \frac{\bar{g}_\theta}{\bar{g}}\sin\left(\frac{m\pi}{\beta}\theta\right)\right]\right\}$$

$$\left. - \left(1 - \frac{\bar{b}}{\bar{r}_0}\frac{m\pi}{\beta}\left(1 + \frac{\bar{g}_\theta^2(0)}{\bar{r}_0^2}\right)^{-1/2}\right)\right]$$

$$= -\bar{r}_0^2\left[\left(1 - \frac{\bar{g}^2}{\bar{r}_0^2}\right) + \frac{2\bar{b}}{\bar{r}_0}\frac{\bar{g}}{\bar{r}_0}\left(1 + \frac{\bar{g}_\theta^2}{\bar{g}^2}\right)^{-1/2}\right.$$

$$\left. - \frac{2\bar{b}}{\bar{r}_0}\left(1 + \frac{\bar{g}_\theta^2(0)}{\bar{r}_0^2}\right)^{-1/2}\right]$$

$$+ \bar{U}_E\bar{b}\left[\left(1 + \frac{\bar{g}_\theta^2}{\bar{g}^2}\right)^{-1/2}\left(\frac{\partial\bar{\psi}(\bar{g},\theta)}{\partial\bar{r}} - \frac{\bar{g}_\theta}{\bar{g}^2}\frac{\partial\bar{\psi}(\bar{g},\theta)}{\partial\theta}\right)\right.$$

$$\left. - \left(1 + \frac{\bar{g}_\theta^2(0)}{\bar{r}_0^2}\right)^{-1/2}\frac{\partial\bar{\psi}(\bar{r}_0,0)}{\partial\bar{r}}\right]. \quad (15a)$$

The corresponding potential distribution may be expressed as

$$\bar{\psi} = \frac{I_0(K\bar{r})}{I_0(K\bar{r}_0)} - \sum_{l=1}^{\infty} \gamma'_l \left\{ \frac{I_0(K\bar{r})}{I_0(K\bar{r}_0)} - \frac{I_{l\pi/\beta}(K\bar{r})}{I_{l\pi/\beta}(K\bar{r}_0)} \cos\left(\frac{l\pi}{\beta}\theta\right) \right\}$$

(16)

where γ'_l is given by

$$1 = \frac{I_0(K\bar{g})}{I_0(K\bar{r}_0)} - \sum_{l=1}^{\infty} \gamma'_l \left\{ \frac{I_0(K\bar{g})}{I_0(K\bar{r}_0)} - \frac{I_{l\pi/\beta}(K\bar{g})}{I_{l\pi/\beta}(K\bar{r}_0)} \cos\left(\frac{l\pi}{\beta}\theta\right) \right\}.$$

(16a)

Equation 15a involves c'_m with m unknowns. For solving the same, one may divide θ in 'i' subdivisions. Let $\bar{g}_i$ be the radial component corresponding to each θ_i. This accordingly yields a $m \times i$ system of algebraic equations. Considering equal dimension, N, for both m and i, the system (15a) yields

$$\sum_{m=1}^{N} c'_m f_{mi} = h_i; \quad \text{for } i = 1, 2, \ldots, N$$

(17)

which can be solved by any matrix inversion method.

Also, the volume flow rate per unit area of the cross section is given by the expression

$$Q = \frac{1}{A} \int_A u \, dA = \int_{\theta=0}^{2\pi} \int_{r=0}^{g(\theta)} u(r,\theta) r \, dr \, d\theta \Bigg/ \int_{\theta=0}^{2\pi} \int_{r=0}^{g(\theta)} r \, dr \, d\theta$$

2.2 Approximate solutions

In deriving the approximate solution, we represent the sole effect of electroosmosis through a slip boundary condition (instead of featuring any body force in the momentum equation for the same), and couple the same with the Navier slip condition to obtain an equivalent slip boundary condition considering combined effects of electroosmosis and interfacial slip. Toward illustrating the same, we first consider a case without any imposed pressure gradient (pure electroosmotic flow). With this consideration, the essential mathematical description of the problem is not disturbed, since, one can express the resultant solution as a linear superposition of solutions for pure electroosmotic and pure pressure-driven flow solutions, considering the linearity of the momentum equation in the Stokes flow limit. Expressing the charge density appearing in Eq. 2a in terms of Eq. 6, one may write the momentum equation governing the pure electroosmotic flow in a compact form

$$\nabla^2 \left(u - \frac{\varepsilon E}{\mu} \psi \right) = 0.$$

(18)

Considering variations of the field variables in the surface normal directions only, and applying the conditions $\frac{\partial u}{\partial n} = 0$ and $\frac{\partial \psi}{\partial n} = 0$ at the channel central line, Eq. 18 may be integrated to yield

$$\frac{\partial u}{\partial n} = \frac{\varepsilon E}{\mu} \frac{\partial \psi}{\partial n}.$$

(19)

Integrating Eq. 19 once more and applying the interfacial boundary conditions: $u = b\frac{\partial u}{\partial n}\big|_{\delta V}$ and $\psi = \zeta$, one gets

$$u = \frac{\varepsilon E}{\mu} \left(\psi - \zeta + b\frac{\partial \psi}{\partial n}\bigg|_{\delta V} \right).$$

(20)

Now outside the EDL, we have $u = U_{\text{HS}}$ (i.e., the Helmholtz–Smoluchowski velocity for pure electroosmotic flow in the presence of interfacial slip) and $\psi = 0$. Considering the same, Eq. 20 yields (following Park and Kim 2009)

$$U_{\text{HS}} = -\frac{\varepsilon E}{\mu} \left(\zeta - b\frac{\partial \psi}{\partial n}\bigg|_{\delta V} \right)$$

(21)

which may be considered as an equivalent slip boundary condition for the approximate solution. The corresponding form of momentum equation governing the approximate solution, with an additional incorporation of the pressure gradient, assumes the form:

$$0 = -\nabla p + \mu \nabla^2 u_{\text{app}}.$$

(22)

It can be noted here that there is no electroosmostic body force term in Eq. 22, since the Helmholtz–Smoluchowski velocity already takes care of the electroosmotic flow physics (in an approximate form) through an artificially posed slip boundary condition.

The solution of Eq. 22, coupled with the slip boundary condition given by Eq. 21, can be expressed in terms of a Green's function $G(\mathbf{x}, \mathbf{x}')$ as: $u_{\text{app}} = -\int_{\delta V} U_{HS} \left[G(x, x')|_{\delta V} \right] dS + \oint_V (\nabla p) G(\mathbf{x}, \mathbf{x}') dV$. Since it is not convenient to obtain the Green's function in an arbitrary geometry, we consider an alternative approach to solve the equation. Consistent with the approach for obtaining the exact solutions, we resort to a cylindrical polar coordinate system for that purpose, so that the corresponding governing equation for momentum conservation takes the form

$$\left[\frac{\partial^2}{\partial r^2} + \frac{1}{r} \frac{\partial}{\partial r} + \frac{1}{r^2} \frac{\partial^2}{\partial \theta^2} \right] u_{\text{app}}(r,\theta) = \frac{1}{\mu} \frac{dp}{dz}.$$

(23)

The solution of Eq. 23 obtained using the conditions: u_{app} is finite as $r \to 0$, symmetric about $\theta = 0$, and $\frac{\partial u_{\text{app}}}{\partial \theta} = 0$ at $\theta = \beta$ is given by

$$u_{\text{app}}(r,\theta) = \frac{r^2}{4\mu} \frac{dp}{dz} + \sum_{m=0,1,2,\ldots} a_m r^{\frac{m\pi}{\beta}} \cos\left(\frac{m\pi}{\beta}\theta\right).$$

(24)

After simplification and using the slip boundary condition, this can be written as

$$u_{\text{app}}(r, \theta) = U_{\text{HS}}^0 + \frac{(r^2 - r_0^2)}{4\mu} \frac{dp}{dz}$$
$$+ \sum_{m=1,2,\ldots} a_m \left(r^{\frac{m\pi}{\beta}} \cos\left(\frac{m\pi}{\beta}\theta\right) - r_0^{\frac{m\pi}{\beta}} \right) \quad (24a)$$

where $U_{\text{HS}}^0 = U_{\text{HS}}|_{\theta=0}$ and

$$U_{\text{HS}} = -\frac{\varepsilon E}{\mu}\left[\zeta - b\left(1 + \frac{g_\theta^2}{g^2}\right)^{-1/2}\left(\frac{\partial\psi}{\partial r} - \frac{g_\theta}{g^2}\frac{\partial\psi}{\partial\theta}\right)\Bigg|_{r=g}\right]. \quad (24b)$$

The constants a_m are given by the equation, for $0 \le r \le g(\theta)$, $0 < \theta \le \beta$

$$U_{\text{HS}}(\theta) - U_e^0 = \frac{(g^2 - r_0^2)}{4\mu}\frac{dp}{dz}$$
$$+ \sum_{m=1,2,\ldots} a_m\left(g^{\frac{m\pi}{\beta}}\cos\left(\frac{m\pi}{\beta}\theta\right) - r_0^{\frac{m\pi}{\beta}}\right). \quad (24c)$$

A non-dimensionalization of the above equations yields

$$\bar{u}_{\text{app}}(\bar{r}, \theta) = \bar{U}_{\text{HS}}^0 + \bar{r}_0^2\left(1 - \frac{\bar{r}^2}{\bar{r}_0^2}\right)$$
$$+ \sum_{m=1,2,\ldots} a_m'\left(\left(\frac{\bar{r}}{\bar{r}_0}\right)^{\frac{m\pi}{\beta}}\cos\left(\frac{m\pi}{\beta}\theta\right) - 1\right) \quad (25a)$$

where

$$\bar{U}_{\text{HS}} = \bar{U}_E\left[1 - \bar{b}\left(1 + \frac{\bar{g}_\theta^2}{\bar{g}^2}\right)^{-1/2}\left(\frac{\partial\bar{\psi}}{\partial\bar{r}} - \frac{\bar{g}_\theta}{\bar{g}^2}\frac{\partial\bar{\psi}}{\partial\theta}\right)\Bigg|_{\bar{r}=\bar{g}}\right] \quad (25b)$$

and $a_m' = a_m\frac{\bar{r}_0^{\frac{m\pi}{\beta}}}{\bar{U}_P}$, as governed by the equation

$$\bar{U}_{\text{HS}}(\theta) - \bar{U}_{\text{HS}}^0 = \bar{r}_0^2\left(1 - \frac{\bar{g}^2}{\bar{r}_0^2}\right)$$
$$+ \sum_{m=1,2,\ldots} a_m'\left(\left(\frac{\bar{g}}{\bar{r}_0}\right)^{\frac{m\pi}{\beta}}\cos\left(\frac{m\pi}{\beta}\theta\right) - 1\right). \quad (25c)$$

In this case, the volume flow rate per unit area of the channel cross section is

$$Q_{\text{app}} = \frac{1}{A}\int_A u_{\text{app}}dA$$
$$= \int_{\theta=0}^{2\pi}\int_{r=0}^{g(\theta)} u_{\text{app}}(r, \theta)rdrd\theta \bigg/ \int_{\theta=0}^{2\pi}\int_{r=0}^{g(\theta)} rdrd\theta.$$
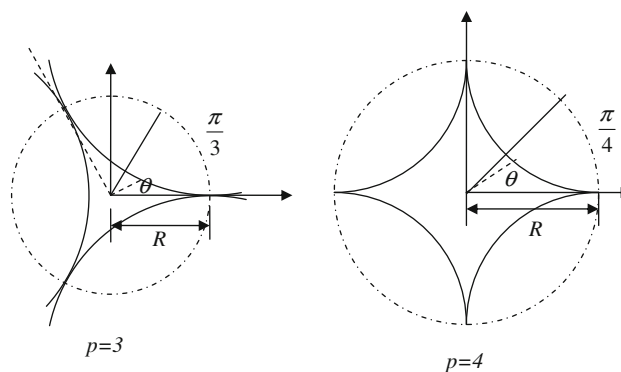

Fig. 2 A schematic illustration of p-point star geometry with $p = 3$ and $p = 4$

After performing the integration with respect to r, the above may be written as

$$Q_{\text{app}} = \int_{\theta=0}^{2\pi} \frac{g^2}{2}\left[U_{\text{HS}}^0 + \frac{1}{4\mu}\frac{dp}{dz}\left(\frac{g^2}{2} - r_0^2\right)\right.$$
$$\left. + \sum_{m=1,2,\ldots} a_m\left(\frac{2g^{\frac{m\pi}{\beta}}}{\frac{m\pi}{\beta}+2}\cos\left(\frac{m\pi}{\beta}\theta\right) - r_0^{\frac{m\pi}{\beta}}\right)\right]d\theta \bigg/ \int_{\theta=0}^{2\pi}\frac{g^2}{2}d\theta$$

2.3 Some special cross-sectional geometries in cylindrical polar coordinates

2.3.1 p-Point star conduit

Figure 2 illustrates typical cross-sectional shapes corresponding to a p-point star conduit. A parametric representation of the concerned geometry is given by

$$\begin{aligned} x &= \frac{R}{p}\{(p-1)\cos(\alpha) + \cos((p-1)\alpha)\} \\ y &= \frac{R}{p}\{(p-1)\sin(\alpha) - \sin((p-1)\alpha)\} \end{aligned}; \quad 0 \le \alpha \le 2\pi. \quad (26)$$

From the above, the sector inside $0 \le \alpha \le \frac{\pi}{p}$ can be written in the polar form as

$$r = \frac{R}{p}\sqrt{\left(1 + (p-1)^2 + 2(p-1)\cos(p\alpha)\right)}$$
$$\theta = \tan^{-1}\left(\frac{(p-1)\sin(\alpha) - \sin((p-1)\alpha)}{(p-1)\cos(\alpha) + \cos((p-1)\alpha)}\right). \quad (27)$$
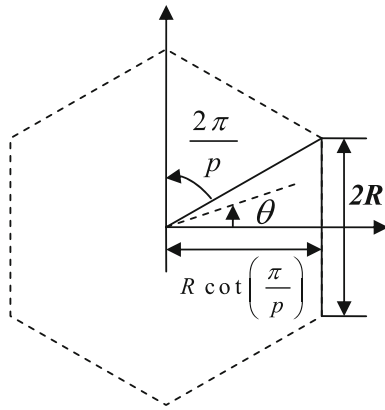
Fig. 3 Schematic illustration of a regular polygon geometry

2.3.2 Regular polygon of side 2R

Figure 3 schematically illustrates the sector of the polygon which lies in $0 \leq \theta \leq \frac{\pi}{p}$. For this geometry, $r = R \cot\left(\frac{\pi}{p}\right) \sec(\theta)$, where p is the number of sides of the polygon.

2.3.3 Elliptic/circular geometry

Figure 4 schematically depicts an elliptical geometry. The equation of an ellipse in polar coordinates, with minor axis 2R and eccentricity e is $r = \frac{R}{\sqrt{1-e^2 \cos^2 \theta}}$; $0 \leq \theta \leq \frac{\pi}{2}$, where $0 < e < 1$ for ellipse and $e = 0$ for circle.

2.4 Illustration of the exact solution (i.e., with exact boundary conditions) and approximate solutions (with approximate boundary conditions) for an annular elliptical geometry

2.4.1 Exact solution

Figure 5 schematically depicts an elliptical cross section with annular geometry, for the sake of illustration of deriving the series solution corresponding to the actual sets of boundary conditions. In this case, the velocity profile, in its general form, reads

$$u(r,\theta) = \frac{r^2}{4\mu}\frac{dp}{dz} + c_1 \ln(r) + c_0 + \frac{\varepsilon E}{\mu}\psi(r,\theta) + \left(a_1 r^\lambda + \frac{a_2}{r^\lambda}\right)\cos(\lambda\theta). \tag{28}$$
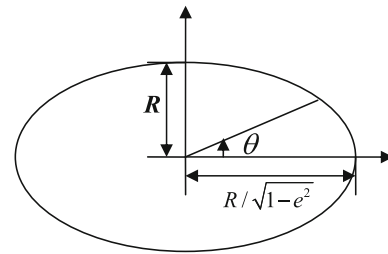

Fig. 4 Schematic illustration of an elliptic geometry

Considering the eigen values, Eq. 28 may be simplified to yield

$$u(r,\theta) = \frac{r^2}{4\mu}\frac{dp}{dz} + c_1 \ln(r) + c_0 + \frac{\varepsilon E}{\mu}\psi(r,\theta)$$
$$+ \sum_{n=1}^{\infty}\left(a_{1n}r^{\frac{n\pi}{\beta}} + a_{2n}r^{-\frac{n\pi}{\beta}}\right)\cos\left(\frac{n\pi}{\beta}\theta\right). \tag{28a}$$

Now applying the boundary conditions

$$u(g_1,\theta) = b_1\left(\sqrt{1 + \frac{g_{1\theta}^2}{g_1^2}}\right)^{-1}\left(\frac{\partial u}{\partial r} - \frac{g_{1\theta}}{g_1^2}\frac{\partial u}{\partial \theta}\right)\Bigg|_{r=g_1} \tag{29a}$$

and

$$u(g_2,\theta) = b_2\left(\sqrt{1 + \frac{g_{2\theta}^2}{g_2^2}}\right)^{-1}\left(\frac{\partial u}{\partial r} - \frac{g_{2\theta}}{g_2^2}\frac{\partial u}{\partial \theta}\right)\Bigg|_{r=g_2} \tag{29b}$$

where b_1 and b_2 are the Navier slip lengths corresponding to the inner and outer surfaces, respectively, we have
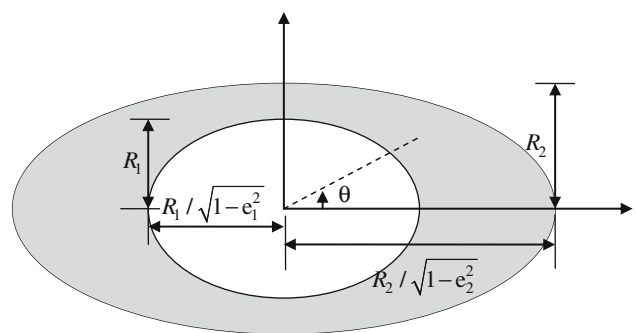

Fig. 5 Schematic depiction of an annular geometry

$$u(r,\theta) = \frac{-g_{10}^2}{4\mu}\frac{dp}{dz}\left(1 - \frac{r}{g_{10}^2}^2\right) + \frac{\varepsilon E\zeta}{\mu}\left(\frac{\psi}{\zeta} - 1\right) + \left\{\frac{\ln\left(\frac{r}{g_{10}}\right) + \frac{b_1}{g_{10}}\left(1 + \frac{g_{1\theta}^2(0)}{g_{10}^2}\right)^{-1/2}}{\ln\left(\frac{g_{20}}{g_{10}}\right) + \frac{b_1}{g_{10}}\left(1 + \frac{g_{1\theta}^2(0)}{g_{10}^2}\right)^{-1/2} - \frac{b_2}{g_{20}}\left(1 + \frac{g_{2\theta}^2(0)}{g_{20}^2}\right)^{-1/2}}\right\}$$

$$\left[\begin{array}{l}\frac{g_{10}^2}{4\mu}\frac{dp}{dz}\left(1 - \frac{g_{20}^2}{g_{10}^2} - \frac{2b_1}{g_{10}}\left(1 + \frac{g_{1\theta}^2(0)}{g_{10}^2}\right)^{-1/2} + \frac{2b_2}{g_{20}}\frac{g_{20}^2}{g_{10}^2}\left(1 + \frac{g_{2\theta}^2(0)}{g_{20}^2}\right)^{-1/2}\right) \\[4mm] \quad + \frac{\varepsilon E\zeta}{\mu}\left[-b_1\frac{\partial\psi(g_{10},0)}{\partial r}\left(1 + \frac{g_{1\theta}^2(0)}{g_{10}^2}\right)^{-1/2} + b_2\frac{\partial\psi(g_{20},0)}{\partial r}\left(1 + \frac{g_{2\theta}^2(0)}{g_{20}^2}\right)^{-1/2}\right] \\[4mm] \quad + \sum_{n=1}^{\infty} a_{1n}g_{10}^{\frac{n\pi}{\beta}}\left[\left\{1 - \frac{b_1}{g_{10}}\frac{n\pi}{\beta}\left(1 + \frac{g_{1\theta}^2(0)}{g_{10}^2}\right)^{-1/2}\right\} - \left(\frac{g_{20}}{g_{10}}\right)^{\frac{n\pi}{\beta}}\left\{1 - \frac{b_2}{g_{20}}\frac{n\pi}{\beta}\left(1 + \frac{g_{2\theta}^2(0)}{g_{20}^2}\right)^{-1/2}\right\}\right] \\[4mm] \quad + \sum_{n=1}^{\infty} a_{2n}g_{10}^{-\frac{n\pi}{\beta}}\left[\left\{1 + \frac{b_1}{g_{10}}\frac{n\pi}{\beta}\left(1 + \frac{g_{1\theta}^2(0)}{g_{10}^2}\right)^{-1/2}\right\} - \left(\frac{g_{20}}{g_{10}}\right)^{-\frac{n\pi}{\beta}}\left\{1 + \frac{b_2}{g_{20}}\frac{n\pi}{\beta}\left(1 + \frac{g_{2\theta}^2 left(0)}{g_{20}^2}\right)^{-1/2}\right\}\right]\end{array}\right]$$

$$+ \sum_{n=1}^{\infty} a_{1n}g_{10}^{\frac{n\pi}{\beta}}\left[\left(\frac{r}{g_{10}}\right)^{\frac{n\pi}{\beta}}\cos\left(\frac{n\pi}{\beta}\theta\right) - \left\{1 - \frac{b_1}{g_{10}}\frac{n\pi}{\beta}\left(1 + \frac{g_{1\theta}^2(0)}{g_{10}^2}\right)^{-1/2}\right\}\right]$$

$$+ \sum_{n=1}^{\infty} a_{2n}g_{10}^{-\frac{n\pi}{\beta}}\left[\left(\frac{r}{g_{10}}\right)^{-\frac{n\pi}{\beta}}\cos\left(\frac{n\pi}{\beta}\theta\right) - \left\{1 + \frac{b_1}{g_{10}}\frac{n\pi}{\beta}\left(1 + \frac{g_{1\theta}^2(0)}{g_{10}^2}\right)^{-1/2}\right\}\right]. \tag{30}$$

In non-dimensional form the above can be re-written as

$$\bar{u}(\bar{r},\theta) = \bar{g}_{10}^2\left(1 - \frac{\bar{r}^2}{\bar{g}_{10}^2} - \frac{2\bar{b}_1}{\bar{g}_{10}}\left(1 + \frac{\bar{g}_{1\theta}^2(0)}{\bar{g}_{10}^2}\right)^{-1/2}\right) - \bar{U}_E\left(\bar{\psi} - 1 + \bar{b}_1\frac{\partial\bar{\psi}(\bar{g}_{10},0)}{\partial\bar{r}}\left(1 + \frac{\bar{g}_{1\theta}^2(0)}{\bar{g}_{10}^2}\right)^{-1/2}\right)$$

$$+ \left\{\frac{\ln\left(\frac{\bar{r}}{\bar{g}_{10}}\right) + \frac{\bar{b}_1}{\bar{g}_{10}}\left(1 + \frac{\bar{g}_{1\theta}^2(0)}{\bar{g}_{10}^2}\right)^{-1/2}}{\ln\left(\frac{\bar{g}_{20}}{\bar{g}_{10}}\right) + \frac{\bar{b}_1}{\bar{g}_{10}}\left(1 + \frac{\bar{g}_{1\theta}^2(0)}{\bar{g}_{10}^2}\right)^{-1/2} - \frac{\bar{b}_2}{\bar{g}_{20}}\left(1 + \frac{\bar{g}_{2\theta}^2(0)}{\bar{g}_{20}^2}\right)^{-1/2}}\right\}$$

$$\times\left[\begin{array}{l}-\bar{g}_{10}^2\left(1 - \frac{\bar{g}_{20}^2}{\bar{g}_{10}^2} - \frac{2\bar{b}_1}{\bar{g}_{10}}\left(1 + \frac{\bar{g}_{1\theta}^2(0)}{\bar{g}_{10}^2}\right)^{-1/2} + \frac{2\bar{b}_2}{\bar{g}_{20}}\frac{\bar{g}_{20}^2}{\bar{g}_{10}^2}\left(1 + \frac{\bar{g}_{2\theta}^2(0)}{\bar{g}_{20}^2}\right)^{-1/2}\right) \\[4mm] \quad + \bar{U}_E\left[\bar{b}_1\frac{\partial\bar{\psi}(\bar{g}_{10},0)}{\partial\bar{r}}\left(1 + \frac{\bar{g}_{1\theta}^2(0)}{\bar{g}_{10}^2}\right)^{-1/2} - \bar{b}_2\frac{\partial\bar{\psi}(\bar{g}_{20},0)}{\partial\bar{r}}\left(1 + \frac{\bar{g}_{2\theta}^2(0)}{\bar{g}_{20}^2}\right)^{-1/2}\right] \\[4mm] \quad + \sum_{n=1}^{\infty} a'_{1n}\left[\left\{1 - \frac{\bar{b}_1}{\bar{g}_{10}}\frac{n\pi}{\beta}\left(1 + \frac{\bar{g}_{1\theta}^2(0)}{\bar{g}_{10}^2}\right)^{-1/2}\right\} - \left(\frac{\bar{g}_{20}}{\bar{g}_{10}}\right)^{\frac{n\pi}{\beta}}\left\{1 - \frac{\bar{b}_2}{\bar{g}_{20}}\frac{n\pi}{\beta}\left(1 + \frac{\bar{g}_{2\theta}^2(0)}{\bar{g}_{20}^2}\right)^{-1/2}\right\}\right] \\[4mm] \quad + \sum_{n=1}^{\infty} a'_{2n}\left[\left\{1 + \frac{\bar{b}_1}{\bar{g}_{10}}\frac{n\pi}{\beta}\left(1 + \frac{\bar{g}_{1\theta}^2(0)}{\bar{g}_{10}^2}\right)^{-1/2}\right\} - \left(\frac{\bar{g}_{20}}{\bar{g}_{10}}\right)^{-\frac{n\pi}{\beta}}\left\{1 + \frac{\bar{b}_2}{\bar{g}_{20}}\frac{n\pi}{\beta}\left(1 + \frac{\bar{g}_{2\theta}^2(0)}{\bar{g}_{20}^2}\right)^{-1/2}\right\}\right]\end{array}\right]$$

$$+ \sum_{n=1}^{\infty} a'_{1n}\left[\left(\frac{\bar{r}}{\bar{g}_{10}}\right)^{\frac{n\pi}{\beta}}\cos\left(\frac{n\pi}{\beta}\theta\right) - \left\{1 - \frac{\bar{b}_1}{\bar{g}_{10}}\frac{n\pi}{\beta}\left(1 + \frac{\bar{g}_{1\theta}^2(0)}{\bar{g}_{10}^2}\right)^{-1/2}\right\}\right]$$

$$+ \sum_{n=1}^{\infty} a'_{2n}\left[\left(\frac{\bar{r}}{\bar{g}_{10}}\right)^{-\frac{n\pi}{\beta}}\cos\left(\frac{n\pi}{\beta}\theta\right) - \left\{1 + \frac{\bar{b}_1}{\bar{g}_{10}}\frac{n\pi}{\beta}\left(1 + \frac{\bar{g}_{1\theta}^2(0)}{\bar{g}_{10}^2}\right)^{-1/2}\right\}\right]. \tag{30a}$$

Here, $\bar{g}_{i0} = \bar{g}_i(0)$, $\bar{g}_{i\theta} = \frac{d\bar{g}_i}{d\theta}$ for $i = 1, 2$, and the constants $a'_{1n} = \frac{a_{1n}}{U_P}\bar{g}_{10}^{\frac{n\pi}{\beta}}$ and $a'_{2n} = \frac{a_{2n}}{U_P}\bar{g}_{10}^{-\frac{n\pi}{\beta}}$ are found using the boundary conditions

$$\bar{u}(\bar{g}_1, \theta) = \bar{b}_1 \left(\sqrt{1 + \frac{\bar{g}_{1\theta}^2}{\bar{g}_1^2}} \right)^{-1} \left(\frac{\partial \bar{u}}{\partial \bar{r}} - \frac{\bar{g}_{1\theta}}{\bar{g}_1^2} \frac{\partial \bar{u}}{\partial \theta} \right) \Bigg|_{\bar{r}=\bar{g}_1} \quad (30b)$$

$$\bar{u}(\bar{g}_2, \theta) = \bar{b}_2 \left(\sqrt{1 + \frac{\bar{g}_{2\theta}^2}{\bar{g}_2^2}} \right)^{-1} \left(\frac{\partial \bar{u}}{\partial \bar{r}} - \frac{\bar{g}_{2\theta}}{\bar{g}_2^2} \frac{\partial \bar{u}}{\partial \theta} \right) \Bigg|_{\bar{r}=\bar{g}_2}. \quad (30c)$$

The above formulation yields a system of $2N \times 2N$ algebraic equations at the boundary points $(\bar{g}_1(\theta_i), \theta_i)$ and $(\bar{g}_2(\theta_i), \theta_i)$ for $i = 1, 2, \ldots, N$. The potential distribution consistent with these equations in non-dimensional form and within thin EDL limits is given by (following Tsao 2000) where $A'_l = \frac{A_l I_{l\pi/\beta}(K\bar{g}_{10})}{\zeta}$, $B'_l = \frac{B_l K_{l\pi/\beta}(K\bar{g}_{10})}{\zeta}$ are

$$\bar{u}_{\text{app}} - \bar{U}_{\text{HS}}^{10} = \bar{g}_{10}^2 \left(1 - \frac{\bar{r}^2}{\bar{g}_{10}^2} \right)$$
$$+ \sum_{n=1}^{\infty} \left\{ a'_{1n} \left[\left(\frac{\bar{r}}{\bar{g}_{10}} \right)^{\frac{n\pi}{\beta}} \cos\left(\frac{n\pi}{\beta}\theta \right) - 1 \right] \right.$$
$$+ a'_{2n} \left[\left(\frac{\bar{r}}{\bar{g}_{10}} \right)^{-\frac{n\pi}{\beta}} \cos\left(\frac{n\pi}{\beta}\theta \right) - 1 \right] \right\}$$
$$+ \frac{\ln\left(\frac{\bar{r}}{\bar{g}_{10}} \right)}{\ln\left(\frac{\bar{g}_{20}}{\bar{g}_{10}} \right)} \left[\left(\bar{U}_{\text{HS}}^{20} - \bar{U}_{\text{HS}}^{10} \right) - \bar{g}_{10}^2 \left(1 - \frac{\bar{g}_{20}^2}{\bar{g}_{10}^2} \right) \right.$$
$$+ \sum_{n=1}^{\infty} \left[a'_{1n} \left\{ 1 - \left(\frac{\bar{g}_{20}}{\bar{g}_{10}} \right)^{\frac{n\pi}{\beta}} \right\} + a'_{2n} \left\{ 1 - \left(\frac{\bar{g}_{20}}{\bar{g}_{10}} \right)^{-\frac{n\pi}{\beta}} \right\} \right] \Bigg]$$
$$(32)$$

$$\bar{\psi} = \left[\frac{K_0(K\bar{g}_{20})}{K_0(K\bar{g}_{10})} - \frac{I_0(K\bar{g}_{20})}{I_0(K\bar{g}_{10})} \right]^{-1} \left[\frac{I_0(K\bar{r})}{I_0(K\bar{g}_{10})} \left[\frac{K_0(K\bar{g}_{20})}{K_0(K\bar{g}_{10})} - 1 \right] - \frac{K_0(K\bar{r})}{K_0(K\bar{g}_{10})} \left[\frac{I_0(K\bar{g}_{20})}{I_0(K\bar{g}_{10})} - 1 \right] \right]$$

$$+ \sum_{l=1}^{\infty} A'_l \begin{bmatrix} \frac{I_{l\pi/\beta}(K\bar{r})}{I_{l\pi/\beta}(K\bar{g}_{10})} \cos\left(\frac{l\pi}{\beta}\theta \right) + \frac{I_0(K\bar{r})}{I_0(K\bar{g}_{10})} \left\{ \frac{I_{l\pi/\beta}(K\bar{g}_{20})}{I_{l\pi/\beta}(K\bar{g}_{10})} - \frac{K_0(K\bar{g}_{20})}{K_0(K\bar{g}_{10})} \right\} \left[\frac{K_0(K\bar{g}_{20})}{K_0(K\bar{g}_{10})} - \frac{I_0(K\bar{g}_{20})}{I_0(K\bar{g}_{10})} \right]^{-1} \\ - \frac{K_0(K\bar{r})}{K_0(K\bar{g}_{10})} \left\{ \frac{I_{l\pi/\beta}(K\bar{g}_{20})}{I_{l\pi/\beta}(K\bar{g}_{10})} - \frac{I_0(K\bar{g}_{20})}{I_0(K\bar{g}_{10})} \right\} \left[\frac{K_0(K\bar{g}_{20})}{K_0(K\bar{g}_{10})} - \frac{I_0(K\bar{g}_{20})}{I_0(K\bar{g}_{10})} \right]^{-1} \end{bmatrix}$$

$$+ \sum_{l=1}^{\infty} B'_l \begin{bmatrix} \frac{K_{l\pi/\beta}(K\bar{r})}{K_{l\pi/\beta}(K\bar{g}_{10})} \cos\left(\frac{l\pi}{\beta}\theta \right) + \frac{I_0(K\bar{r})}{I_0(K\bar{g}_{10})} \left\{ \frac{K_{l\pi/\beta}(K\bar{g}_{20})}{K_{l\pi/\beta}(K\bar{g}_{10})} - \frac{K_0(K\bar{g}_{20})}{K_0(K\bar{g}_{10})} \right\} \left[\frac{K_0(K\bar{g}_{20})}{K_0(K\bar{g}_{10})} - \frac{I_0(K\bar{g}_{20})}{I_0(K\bar{g}_{10})} \right]^{-1} \\ - \frac{K_0(K\bar{r})}{K_0(K\bar{g}_{10})} \left\{ \frac{K_{l\pi/\beta}(K\bar{g}_{20})}{K_{l\pi/\beta}(K\bar{g}_{10})} - \frac{I_0(K\bar{g}_{20})}{I_0(K\bar{g}_{10})} \right\} \left[\frac{K_0(K\bar{g}_{20})}{K_0(K\bar{g}_{10})} - \frac{I_0(K\bar{g}_{20})}{I_0(K\bar{g}_{10})} \right]^{-1} \end{bmatrix} \quad (31)$$

constants determined from the boundary condition $\bar{\psi} = 1$ at the boundaries $\bar{r} = \bar{g}_1$ and $\bar{r} = \bar{g}_2$.

2.5 Approximate solution

Following the approximate situation, the velocity distribution inside the annular region $\{\bar{g}_1(\theta) \leq \bar{r} \leq \bar{g}_2(\theta); 0 \leq \theta \leq \beta\}$ is given as

where $\bar{U}_{\text{HS}}^{10}, \bar{U}_{\text{HS}}^{20}$ are the values of the modified Smoluchowski slip velocities at the point $\theta = 0$, which are given by, at the boundaries $\bar{r} = \bar{g}_1(\theta)$ and $\bar{r} = \bar{g}_2(\theta)$,

$$\bar{U}_{HS}^j = \bar{U}_E \left(1 - \bar{b}_j (\nabla\bar{\psi} \cdot \hat{\mathbf{n}}_j)\big|_{\bar{r}=\bar{g}_j(\theta)} \right); j = 1, 2 \quad (33)$$

where $\hat{\mathbf{n}}_j$ is the unit normal at the boundary $\bar{r} = \bar{g}_j(\theta)$. The constants a'_{1n} and a'_{2n} are determined from the equations for $0 < \theta \leq \beta$ and $j = 1, 2$

$$\bar{U}_{\text{HS}}^{j} - \bar{U}_{\text{HS}}^{10} = \bar{g}_{10}^2 \left(1 - \frac{\bar{g}_j^2(\theta)}{\bar{g}_{10}^2}\right) + \frac{\ln\left(\frac{\bar{g}_j(\theta)}{\bar{g}_{10}}\right)}{\ln\left(\frac{\bar{g}_{20}}{\bar{g}_{10}}\right)}\left[(\bar{U}_{\text{HS}}^{20} - \bar{U}_{\text{HS}}^{10})\right.$$

$$- \bar{g}_{10}^2 \left(1 - \frac{\bar{g}_{20}^2}{\bar{g}_{10}^2}\right)\right] + \frac{\ln\left(\frac{\bar{g}_j(\theta)}{\bar{g}_{10}}\right)}{\ln\left(\frac{\bar{g}_{20}}{\bar{g}_{10}}\right)} \left[\sum_{n=1}^{\infty}\left[a_{1n}'\left\{1 - \left(\frac{\bar{g}_{20}}{\bar{g}_{10}}\right)^{\frac{n\pi}{\beta}}\right\}\right.\right.$$

$$+ a_{2n}'\left\{1 - \left(\frac{\bar{g}_{20}}{\bar{g}_{10}}\right)^{-\frac{n\pi}{\beta}}\right\}\right]\right]$$

$$+ \sum_{n=1}^{\infty} a_{1n}'\left[\left(\frac{\bar{g}_j(\theta)}{\bar{g}_{10}}\right)^{\frac{n\pi}{\beta}}\cos\left(\frac{n\pi}{\beta}\theta\right) - 1\right]$$

$$+ \sum_{n=1}^{\infty} a_{2n}'\left[\left(\frac{\bar{g}_j(\theta)}{\bar{g}_{10}}\right)^{-\frac{n\pi}{\beta}}\cos\left(\frac{n\pi}{\beta}\theta\right) - 1\right]. \qquad (34)$$

In both the cases, the volume flow rates Q and Q_{app} can be found by integrating u and u_{app} (as given in Eqs. 30 and 32), respectively, over the region $\{g_1(\theta) \leq r \leq g_2(\theta); 0 \leq \theta \leq \beta\}$.

3 Illustrative case studies

We assess the validity of the approximate solution obtained through the employment of the effective slip boundary condition by comparing the same with the exact solution obtained by a detailed modeling of the electro-hydrodynamic transport within the EDL. Figure 6 compares the ratio of the flow rate obtained by the approximate solution as compared to that obtained from the exact solution $\left(Q_{\text{app}}/Q\right)$, as a function of the relative EDL thickness ($K = \kappa D_{\text{h}}$, i.e., Debye length relative to the channel hydraulic diameter), for different channel cross-sectional geometries. It is important to note in this context that the authenticity of the exact solutions obtained in the present solution is otherwise comprehensively verified with the full scale numerical solutions of the pertinent electro-hydrodynamic equations, using a control volume-based conservative numerical framework (not detailed here for the sake of brevity). The results are presented here as parametric functions of the dimensionless slip length (i.e., slip length
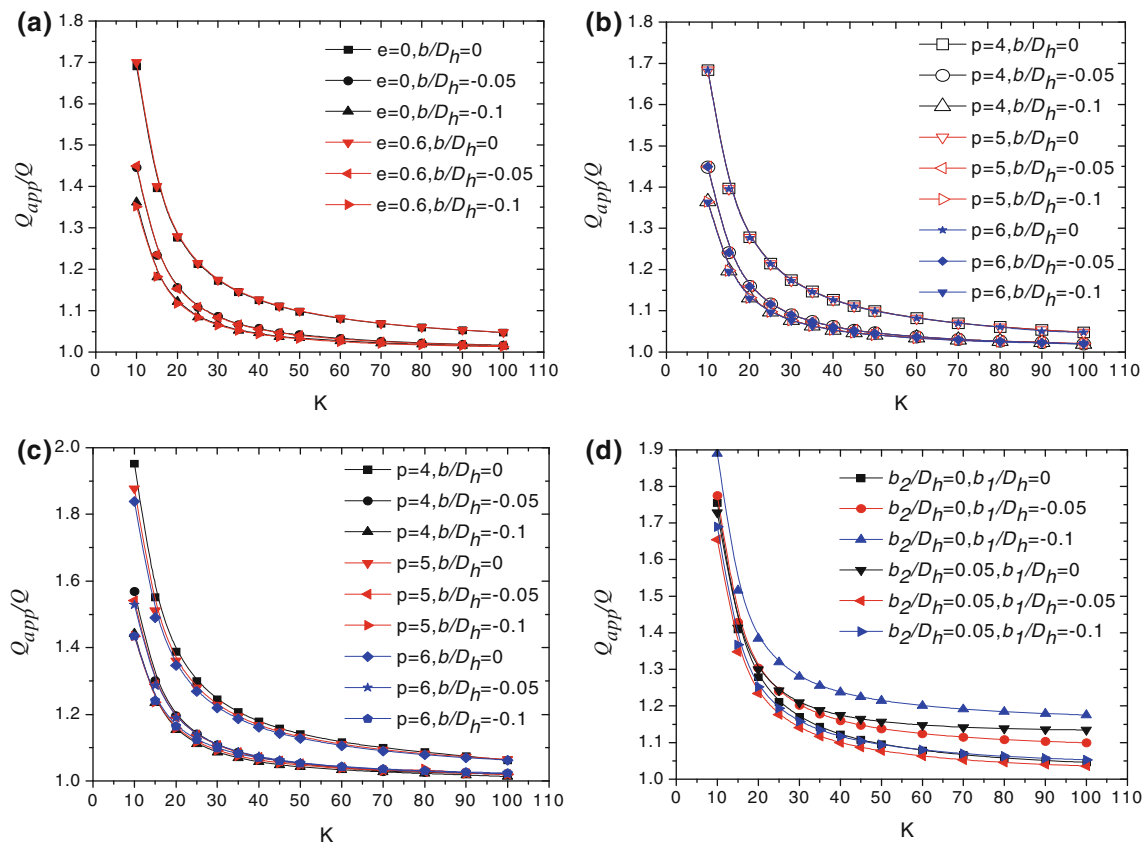

Fig. 6 Ratio of volume flow rate as predicted by the approximate and exact solutions with respect to the non-dimensional EDL thickness, corresponding to different values of slip length, for **a** circular ($e = 0$) and elliptic ($e = 0.6$) geometry, **b** polygonal geometry, **c** point star geometry, taking $\bar{U}_E = -1$, and **d** circular annulus with different b_1 and b_2, taking $R_1 = \frac{1}{2}R_2$ and $\bar{U}_E = -1$

normalized relative to the hydraulic diameter). From Fig. 6a, it is evident that the approximate solution for flow rate overpredicts the flow rate by a factor that increases dramatically as the value of K decreases below a threshold limit. This threshold limit, interestingly, is sensitively dependent on the magnitude of the Navier slip length. Higher the magnitude of the slip length, less turns out to be the deviation of the flow rate predicted by the approximate solution from that predicted by the exact solution. The general trend of the approximate solution overpredicting the exact solution (concerning the flow rate) stems from the fact that the approximate solution does not effectively capture the velocity gradient within the EDL. Thicker the EDL relative to the channel hydraulic diameter (i.e., smaller the value of K), more significant is the implication of this error, because of a deficit in the calculated momentum transport over a more extended portion of the sub-domain adjacent to the solid boundaries. This leads the error to shoot up as the characteristic EDL thickness approaches the channel hydraulic radius. However, a higher extent of Navier slip within the EDL tends to compensate for this momentum deficit to a more significant extent, so that the error gets nullified to a large proportion. Accordingly, more dominant the mechanism of interfacial (Navier) slip, less turns out to be the error incurred due to neglecting the velocity gradients within the EDL, as attributable to a greater prominence of slipping hydrodynamics within the EDL. It is also important to mention in this context that, with relatively thicker EDLs (EDL size approaching the hydraulic radius in order), EDLs from different portions of the domain boundary tend to interfere with each other, so that the exact solution presented in this article itself becomes vulnerable. Such cases occur below $K \sim O(1)$, and are not considered in this study. When such conditions do not occur, the present methodology is capable of generating very accurate solutions for the flow rate even for very complicated geometries, as evident from Fig. 6. Regarding the effect of the channel geometry on the error concerning the flow solution, it may be inferred that less the eccentricity of the channel section, more is the concerned error. Analogous inferences can be drawn from Fig. 6b, concerning a polygonal geometry of the channel section. In such cases, the error in the approximate solution increases as the number of sides of the polygon increases, since error for each side is effectively cumulated. This can be extrapolated to the fact that the error is maximum for a circular geometry (see Fig. 6a), as dictated by the fact that the circle in effectively a regular p-sided polygon with $p \to \infty$. Similar conclusions can be drawn for p-point star geometries (Fig. 6c) and also for annular sections (Fig. 6d). In Fig. 6d, the flow rate ratio is depicted as a function of the relative EDL thickness, for different ratios of the inner to outer circle radius, corresponding to the

special case of an annular circular geometry ($e_1 = e_2 = 0$). Interestingly, it is revealed for that case that the Q_{app}/Q versus K characteristics are independent of the absolute values of the inner and the outer radius but are solely dependant on the ratio of these two dimensions, while other conditions remaining unaltered, as attributable to an invariance of the solutions with respect to similarities in the flow geometry. To generalize, the ratio Q_{app}/Q turns out to be an intrinsic characteristic of the shape of the microchannel section, regardless of the absolute values of the pertinent geometrical dimensions, so long as the other influencing physical parameters remain unaltered. Thus, the Q_{app}/Q characteristics presented in this study depict universal signatures of electroosmotically driven microchannel flows occurring through various complicated-shaped cross sections with interfacial slip, disregarding the absolute cross-sectional dimensions but very much specific to the channel cross-sectional shapes. These characteristics also essentially focus on the extent to which the thin EDL limit assumptions may be valid for flow rate computations in the presence of hydrophobic interactions, as a sensitive parametric function of the relative EDL thickness with respect to the channel hydraulic diameter, for different channel sections. Such signature characteristics, in turn, may be immensely useful for designing microchannels with complex cross sections for desired flow rate variations under a given driving influence, consistent with the system requirements, in the presence of hydrophobic interactions characterized with interfacial slip.

4 Conclusion

In this article, we first derive exact solutions for electroosmotic flows in microchannels in the presence of Navier slip (expressed by a Navier slip-based boundary condition), corresponding to microchannel geometries with complex cross-sectional shapes. The study is primarily motivated by the fact that microfabrication artifacts commonly result in microchannel geometries with cross sections significantly deviated from the routinely presumed rectangular and circular ones. In addition, the narrow flow passages in packed beds assume more complicated cross-sectional shapes. Further to these considerations, we also derive more simplified approximate solutions, using the concept of extended Helmholtz–Smoluchowski velocity for hydrophobic microchannels with Navier slip. Results from the approximate solution, with regard to flow rate predictions, turn out to be in good agreement with those obtained by solving the exact equations composed of the Navier–Stokes equation and the Poisson–Boltzmann equation for non-overlapping

EDLs. However, as the EDL thickness approaches the channel hydraulic radius (typical to nanochannels), the error tends to get magnified to significant proportions. Interestingly, higher is the velocity slip, closer turns out to be the agreement between the approximate and the exact solutions. Such conclusions are found to be explicit functions of the channel cross-sectional shape, disregarding the actual dimensions, provided other physical parameters governing the flow remain unaltered. The semi-analytical formulations outlined in this study, thus, are expected to generalize the design and analysis of various lab-chip-based microfluidic devices of complex cross-sectional shapes, in which electroosmotic flow occurs in the presence of interfacial slip.

References

Bonaccurso E, Butt HJ, Craig VSJ (2003) Surface roughness and hydrodynamic boundary slip of a Newtonian fluid in a completely wetting system. Phys Rev Lett 90:144501

Bruin GJM (2000) Recent developments in electrokinetically driven analysis on micro-fabricated devices. Electrophoresis 21:3931–3951

Bruus H (2008) Theoretical microfluidics. Oxford University Press, Oxford

Chakraborty S (2008) Generalization of interfacial electrohydrodynamics in the presence of hydrophobic interactions in narrow fluidic confinements. Phys Rev Lett 100:097801

Dolnik V, Hutterer KM (2001) Capillary electrophoresis of proteins 1999–2001. Electrophoresis 22:4163–4178

Duan Z, Muzychka YS (2007) Slip flow in elliptic microchannels. Int J Therm Sci 46:1104–1111

Figeys D, Pinto D (2001) Proteomics on a chip: promising developments. Electrophoresis 22:208–216

Galea TM, Attard P (2004) Molecular dynamics study of the effect of atomic roughness on the slip length at the fluid–solid boundary during shear flow. Langmuir 20:3477

Hunter RJ (2000) Foundations of colloid science, 2nd edn. Oxford University Press, Oxford

Joly L, Ybert C, Trizac E, Bocquet L (2004) Hydrodynamics within the electric double layer on slipping surfaces. Phys Rev Lett 93:257805

Landers JP (2003) Molecular diagnostics on electrophoretic microchips. Anal Chem 75:2919–2927

Li D (2004) Electrokinetics in microfluidics. Elsevier, Amsterdam

Park HM, Kim TW (2009) Extension of the Helmholtz–Smoluchowski velocity to the hydrophobic microchannels with velocity slip. Lab Chip 9:291–296

Park HM, Lim JY (2009) Streaming potential for microchannels of arbitrary cross-sectional shapes for thin electric double layers. J Colloid Interface Sci 336:834–841

Reyes DR, Iossifidis D, Auroux PA, Manz A (2002) Micro total analysis systems. 1. Introduction, theory, and technology. Anal Chem 74:2623–2636

Shih FS (1967) Laminar flow in axisymmetric conduits by a rational approach. Can J Chem Eng 45:285–294

Stone HA, Kim S (2001) Microfluidics: basic issues, applications, and challenges. AIChE J 47:1250–1254

Tsao HK (2000) Electroosmotic flow through an annulus. J Colloid Interface Sci 225:247–250

Whitesides GM, Stroock AD (2001) Flexible methods for microfluidics. Phys Today 54:42–48

Yang J, Kwok DY (2002) A new method to determine zeta potential and slip coefficient simultaneously. J Phys Chem B106:12851–12855

Yang J, Kwok DY (2003) Microfluid flow in circular microchannel with electrokinetic effects and Navier's slip condition. Langmuir 19:1047–1053

Yang J, Kwok DY (2004) Analytical treatment of electrokinetic microfluidics in hydrophobic microchannels. Anal Chim Acta 507:39–53

Zhang Y, Wong TN, Yang C, Ooi KT (2005) Electroosmotic flow in irregular shape microchannels. Int J Eng Sci 43:1450–1463

Zhu Y, Granick S (2002) Limits of the hydrodynamic no-slip boundary condition. Phys Rev Lett 88:106102